Deblurring Subject to Nonnegativity Constraints When Known Functions Are Present With Application to Object-Constrained Computerized Tomography

Donald L. Snyder*, *Fellow, IEEE,* Joseph A. O'Sullivan, *Senior Member, IEEE*, Bruce R. Whiting, Ryan J. Murphy, Jasenka Benac, *Student Member, IEEE,* J. Adam Cataldo, David G. Politte, *Member, IEEE,* and Jeffrey F. Williamson

***Abstract*—The reconstruction of tomographic images is often treated as a linear deblurring problem. When a high-density, man-made metal object is present somewhere in the image field, it is a deblurring problem in which the unknown function has a component that is known except for some location and orientation parameters. We first address general linear deblurring problems in which a known function having unknown parameters is present. We then show how the resulting iterative solution can be applied to tomographic imaging in the presence of man-made foreign objects, and we apply the result, in particular, to X-ray computed tomography imaging used in support of brachytherapy treatment of advanced cervical cancer.**

***Index Terms*—Brachytherapy, cervical cancer, computerized tomography, metal artifacts, tomography.**

I. Introduction

OUR OBJECTIVE is to define and provide a solution to a linear, deterministic, deblurring problem and then to indicate how the solution may be used. The results have a wide range of possible applications. We illustrate one such application: X-ray tomographic imaging used in support of brachytherapy treatment of locally advanced cervical cancer. In doing so, a new image reconstruction method is identified that we call *object-constrained computerized tomography* (OCCT).

Linear deblurring problems arise when measured data are modeled as a linear transformation of an unknown function, where the transformation is characterized by a known kernel (i.e., point-spread function), and the unknown function is sought. Deconvolution problems are a special case when the kernel is time or space invariant. Approaches for solving many types of deblurring problems are widely discussed in the literature; for example, see the book by Stark [23] and references therein. We limit ourselves to deblurring problems in which the data, kernel, and unknown function are each constrained to be nonnegative. Solution approaches in the presence of such a constraint are developed by Youla [30] based on a least-squares discrepancy-measure and by Snyder *et al.* [21] based on a divergence discrepancy-measure (see also [1] and [25]). Using information-theoretic arguments, O'Sullivan [12] discusses alternating minimization algorithms that include this problem. The approach we use here falls within the general framework of information-theoretic image formation described by O'Sullivan *et al.* [13].

The novel aspect of the deblurring problem that we now address is that, in addition to the nonnegativity constraint, the unknown function has a component with a known form but which contains unknown parameters. We develop a solution based on a divergence discrepancy-measure.

Our motivation for formulating the deblurring problem in the context of X-ray tomography is that filtered backprojection (FBP), which is the almost universally used method of image reconstruction, produces images that are highly artifactual when high-density objects are inside the body. The artifacts often take the form of alternating light and dark stripes of high amplitude in a star-burst pattern extending across the entire image and masking many details that may be of interest. For this reason, X-ray tomographic images intended to visualize soft tissues in the vicinity of prosthetic implants, surgical clips, spinal rods, cochlear implants, brachytherapy applicators, etc., are of greatly diminished or no clinical value when formed from projection data by FBP. This difficulty is discussed by Fiala *et al.* [4], Kalender *et al.* [7], DeMan *et al.* [3], Marks and Callen [11], Robertson *et al.* [18], Strumas *et al.* [24], and by many others.

Image reconstruction methods designed to reduce artifacts when high-density metallic objects are present have been described by Glover and Pelc [6], Kalender *et al.* [7], Lonn and Crawford [10], Klotz and Kalender [8], Rohlfing *et al.* [19], Weeks [27], Wang *et al.* [26], and Gebara *et al.* [5]. In Kalender's method, portions of projection data that are missing or highly attenuated, presumably due to attenuation by a very high-density metal object, are estimated by linear interpolation across missing portions of each projection. Images are then formed from the modified projection data via FBP. While these methods may work adequately in some circumstances, our preliminary evaluations of the new method we shall describe indicate that valuable improvements are possible. A precursor [26] of the new approach we will describe does not use FBP;

Manuscript received July 17, 2000; revised July 31, 2001. This work was supported in part by Washington University. The work of J. F. Williamson was supported by the National Institutes of Health under Grant R01CA75371 from the National Cancer Institute of the National Institutes of Health. The Associate Editor responsible for coordinating the review of this paper and recommending its publication was C. Crawford. *Asterisk indicates corresponding author.*

*D. L. Snyder is with the Department of Electrical Engineering, Washington University, Box 1127, St. Louis, MO 63130-4899 USA (e-mail: dls@ee.wustl.edu).

J. A. O'Sullivan, R. J. Murphy, J. Benac, and J. A. Cataldo are with the Department of Electrical Engineering, Washington University, St. Louis, MO 63130-4899 USA.

B. R. Whiting and D. G. Politte are with the Electronic Radiation Laboratory, Washington University, St. Louis, MO 63108 USA.

J. F. Williamson is with the Department of Radiation Oncology, Washington University, St. Louis, MO 63108 USA.

Publisher Item Identifier S 0278-0062(01)09302-8.

rather, it is iterative, requiring more computations. This method enforces nonnegativity of the reconstructed attenuation function. It also permits information about an embedded object to be used. However, such objects must be completely opaque and contained within a convex region at a known location within the body. We remove these limitations by adopting a more model-based approach that permits all that is known about a man-made foreign object in the body to be exploited during the formation of images, including its complicated shape and nonuniform attenuation characteristics. The location and orientation of the object in the body is not presupposed but is determined as an integral and concurrent part of the image-formation process.

II. The Deblurring Problem: Definition

We address the following constrained, linear, deterministic, deblurring problem. A nonnegative function $\{m(y),\, y \in Y\}$ and a nonnegative kernel $\{h(y|x),\, y \in Y,\, x \in X\}$ are given, and a nonnegative function $\{c(x),\, x \in X\}$, satisfying the admissibility constraint defined below, is sought such that the approximation

$$m(y) \approx \sum_{x \in X} h(y|x)c(x) \qquad y \in Y \tag{1}$$

is "good." The left-hand side of (1) denotes measured and logarithmically transformed transmission profiles (or *sinogram data* in CT terminology), while the right side models these data with varying degrees of accuracy. We term the domains X and Y the input (image) and output (sinogram) spaces, respectively; these are discrete sets. $m(\cdot)$ is a measured function, $h(\cdot|\cdot)$ is a known kernel or point-spread function, and $c(\cdot)$ is a function to be determined by solving the linear inverse problem (1). In [21], the unknown function $c(\cdot)$ is assumed to be nonnegative but otherwise arbitrary. Here, this function is assumed to be a superposition of an unknown, nonnegative function $\{c_b(x),\, x \in X\}$ and a nonnegative function $\{c_a(x : \theta),\, x \in X,\, \theta \in \Theta\}$ that describes the shape and composition of a man-made object but contains parameters, represented by θ and having values in a compact parameter set Θ, that are unknown. To define admissible solutions, we introduce the following subsets of the input space X. Let $X_a(\theta)$ be the elements of X that support the function $c_a(\cdot : \theta)$ for parameters θ, and let $X_b(\theta) = X \cap \overline{X}_a(\theta)$ be the complementary set in the input space. Also, let $C(\theta)$ be the set of functions that are zero in $X_a(\theta)$; that is

$$C(\theta) = \{c_b(x),\, x \in X : c_b(x) = 0,\, x \in X_a(\theta)\}. \tag{2}$$

An admissible solution for parameters θ then has the form

$$\begin{aligned} c(x : \theta) &= c_b(x) + c_a(x : \theta) \\ &= \begin{cases} c_b(x), & x \in X_b(\theta),\ c_b(\cdot) \in C(\theta) \\ c_a(x : \theta), & x \in X_a(\theta). \end{cases} \end{aligned} \tag{3}$$

The known function $c_a(\cdot : \theta)$ can be parameterized in various ways that can be selected appropriately to accommodate a given application. For the tomographic-imaging problem we consider, $c_b(\cdot)$ represents body tissues, and $c_a(\cdot : \theta)$ represents a foreign object of known form in a reference coordinate-system, and rotations and translations of it are of interest. Then, we may select $\theta = (R,\, x_0)$, where $(R,\, x_0)$ is a rotation-matrix, translation-vector pair that describes the object in its unknown position according to $c_a(Rx + x_0)$. In two dimensions, we define the rotation matrix R by

$$R = \begin{bmatrix} \cos\alpha & \sin\alpha \\ -\sin\alpha & \cos\alpha \end{bmatrix} \tag{4}$$

so it is parameterized by a single rotation angle α. The translation vector, x_0, is two-dimensional, for a total of three unknown parameters characterizing the position and orientation of the object. In three dimensions, we specify R by three angles $(\alpha,\, \beta,\, \gamma)$, respectively called yaw, pitch, and roll, according to

$$\begin{aligned} R = &\begin{bmatrix} 1 & 0 & 0 \\ 0 & \cos\gamma & \sin\gamma \\ 0 & -\sin\gamma & \cos\gamma \end{bmatrix} \begin{bmatrix} \cos\beta & 0 & -\sin\beta \\ 0 & 1 & 0 \\ \sin\beta & 0 & \cos\beta \end{bmatrix} \\ &\times \begin{bmatrix} \cos\alpha & \sin\alpha & 0 \\ -\sin\alpha & \cos\alpha & 0 \\ 0 & 0 & 1 \end{bmatrix} \end{aligned} \tag{5}$$

and the position vector is three-dimensional (3-D), for a total of six unknown parameters characterizing the position and orientation. Objects having articulating parts or multiple, independent parts can be accommodated but require additional parameters to characterize their position and orientation.

For the reasons outlined in [21], we use Csiszár's I-divergence [2] as a discrepancy measure to identify an admissible function $c(\cdot)$ that approximately satisfies (1).[1] Thus, we seek an admissible estimate $\hat{c}(x) \equiv \hat{c}(x : \hat{\theta}) = \hat{c}_b(x) + c_a(x : \hat{\theta})$ defined for $x \in X$ by

$$\hat{c}(x) = \underset{c,\, \theta : c_b \in C(\theta),\, \theta \in \Theta}{\arg\min}\, I\left[m(\cdot) \left\| \sum_{x' \in X} h(\cdot|x')c(x') \right.\right] \tag{6}$$

where $c(\cdot)$ is given in (3), and

$$\begin{aligned} &I\left[m(\cdot) \left\| \sum_{x \in X} h(\cdot|x)c(x) \right.\right] \\ &\quad = \sum_{y \in Y} m(y) \ln \left[\frac{m(y)}{\sum_{x \in X} h(y|x)c(x)} \right] \\ &\qquad + \sum_{y \in Y} \left[\sum_{x \in X} h(y|x)c(x) - m(y) \right]. \end{aligned} \tag{7}$$

For brevity, we denote $I[m(\cdot)\| \sum_{x \in X} h(\cdot|x)c(x)]$ by $I(c)$. This cost function is unavoidably nonconvex in the quantities to be estimated.

[1] Csiszár addresses the problem of selecting discrepancy measures for comparing two functions. He does this by postulating desirable characteristics such measures should have and then identifies measures having such characteristics. For real-valued functions (i.e., positive and negative), he shows that the only measure consistent with his postulates is squared error. For nonnegative functions, the only such measure is the I-divergence.

III. The Deblurring Problem: Solution

Our solution to (6) is in the form of a sequence of admissible estimates $\{\hat{c}^{(k)}(x), x \in X, k = 0, 1, 2, \ldots\}$, produced recursively. To state the iteration concisely, define the function $P(x|y:\tilde{c})$ as follows:

$$P(x|y:\tilde{c}) = \frac{h(y|x)\tilde{c}(x)}{\sum_{x'} h(y|x')\tilde{c}(x')} \tag{8}$$

where

$$\tilde{c}(x) = c_a\left(x:\tilde{\theta}\right) + \tilde{c}_b(x). \tag{9}$$

Also, define $H_0(x)$ according to

$$H_0(x) = \sum_{y\in Y} h(y|x). \tag{10}$$

The iteration is as follows.

Set $k = 0$, select initial estimates $(\hat{\theta}^{(0)}, \hat{c}_b^{(0)} \in C(\hat{\theta}^{(0)}))$, and form the admissible estimate

$$\hat{c}^{(0)}(x:\theta^{(0)}) = \hat{c}_b^{(0)}(x) + c_a\left(x:\hat{\theta}^{(0)}\right), \quad x \in X. \tag{11}$$

For $k = 0, 1, 2, \ldots$ (continuing until done)

{

$$\hat{c}^{(k+1)}(x:\theta) = \arg\min_{c:\, c_b\in C(\theta)} \left\{ -\sum_{y\in Y}\sum_{x\in X} P\left(x|y:\hat{c}^{(k)}(\cdot)\right) m(y)\ln c(x:\theta) + \sum_{x\in X} H_0(x)c(x:\theta)\right\} \tag{12}$$

$$\hat{\theta}^{(k+1)} = \arg\min_{\theta} \left\{ -\sum_{y\in Y}\sum_{x\in X} P\left(x|y:\hat{c}^{(k)}(\cdot)\right) \cdot m(y)\ln \hat{c}^{(k+1)}(x:\theta) + \sum_{x\in X} H_0(x)\hat{c}^{(k+1)}(x:\theta)\right\} \tag{13}$$

$$\hat{c}^{(k+1)}(x) = \hat{c}^{(k+1)}(x:\hat{\theta}^{(k+1)}). \quad x \in X \tag{14}$$

}

For an interpretation of (12)–(14), suppose that an admissible estimate $\hat{c}^{(k)}(\cdot)$ is available at the completion of step k of the iteration. $P(x|y:\hat{c}^{(k)}(\cdot))$ is evaluated using (8) and used in (12) and (13). Then, (13) requires a search over poses θ until a minimum is achieved; this determines $\hat{\theta}^{(k+1)}$. For each test value of θ in this search for a minimum, $\hat{c}^{(k+1)}(\cdot:\theta)$ is required; this is determined using (12). Then, an admissible image for step $k+1$ of the iteration is determined using (14).

An alternative expression for $\hat{c}^{(k+1)}(x:\theta)$ in (12) is

$$\hat{c}^{(k+1)}(x:\theta) = \arg\min_{c_b\in C(\theta)} \left\{ -\sum_{y\in Y}\sum_{x\in X_b(\theta)} P\left(x|y:\hat{c}^{(k)}(\cdot)\right) m(y)\ln c_b(x) + \sum_{x\in X_b(\theta)} H_0(x)c_b(x)\right\} + c_a(x:\theta). \tag{15}$$

The minimization in (15) and, hence, in (12), is over nonnegative functions and can be performed directly to give

$$\hat{c}^{(k+1)}(x:\theta) = \begin{cases} \hat{c}_{\mathrm{EM}}^{(k+1)}(x), & x \in X_b(\theta) \\ c_a(x:\theta), & x \in X_a(\theta) \end{cases} \tag{16}$$

where

$$\hat{c}_{\mathrm{EM}}^{(k+1)}(x) = \hat{c}^{(k)}(x)\frac{1}{H_0(x)}\sum_{y\in Y}\frac{h(y|x)m(y)}{\sum_{x'} h(y|x')\hat{c}^{(k)}(x')}. \tag{17}$$

Evaluation of (16) requires one forward and one backward projection.

The minimization in (13) must generally be performed numerically. We do this by evaluating the function within braces on the right in (13) for test values of θ on a discrete lattice in the neighborhood of $\hat{\theta}^{(k)}$. The lattice step size is initially one pixel spatially and 1° angularly; if test values for neighbors on a lattice of this step size do not yield a lower value of the function, the step size is reduced by a factor, for example 10, and further test values are attempted. This process continues until a lower function value results, with $\hat{\theta}^{(k+1)}$ then taken to be the test value of θ achieving that lower value. Evaluating (13) requires no forward or backward projections, but the number of test values can vary on each iteration because step sizes can change.

As demonstrated in the Appendix, the sequence of estimates produced by this iteration yields a corresponding sequence of I-divergences that is nonincreasing (and generally decreasing)

$$I(\hat{c}^{(0)}) \geq I(\hat{c}^{(1)}) \geq I(\hat{c}^{(2)}) \geq \cdots. \tag{18}$$

Since, the I-divergence is bounded below by zero, this implies that the sequence of I-divergences converges toward a (local) minimum with increasing k.

IV. Application to Tomographic Imaging

Application requires that the input, output, and parameter spaces, X, Y, and Θ, and the kernel, $h(y|x)$, in (1) be identified. Choices that are appropriate for tomographic imaging depend on the tomograph's data-acquisition format and the method of discretization adopted for the input and output spaces and the point-spread function. Data can be in a variety of formats corresponding to: parallel-beam, translate-rotate geometry; fan-beam, planar geometry; fan-beam, helical-scan geometry

for single-row or multirow detectors; or cone-beam geometry. $\tilde{X} \subseteq \mathbf{R}^2$ and $\tilde{Y} = \mathbf{R}^1 \times [0, \pi)$ for a parallel-beam geometry, with $x = (x_1, x_2) \in \tilde{X}$ parameterizing a location in the attenuation density to be imaged, and $y = (t, \varphi) \in \tilde{Y}$ parameterizing a projection ray by its perpendicular distance from the origin and its angular orientation relative to a coordinate axis. A planar, fan-beam geometry is shown in Fig. 1. For this, $\tilde{X} \subseteq \mathbf{R}^2$ and $\tilde{Y} = [0, 2\pi) \times [-\gamma_m, \gamma_m]$, where $\pm\gamma_m$ is the angular extent of the beam, with $y = (\beta, \gamma) \in \tilde{Y}$ parameterizing a projection ray, where β is the source angle, γ is the angle of the ray in the fan, and D is the radial distance of the X-ray source from the axis of rotation. For a helical-scan, fan-beam geometry, $\tilde{X} \subseteq \mathbf{R}^3$ and $\tilde{Y} = [0, 2\pi n] \times [-\gamma_m, \gamma_m]$, where n is the number of source revolutions, $x = (x_1, x_2, x_3) \in \tilde{X}$, and a projection ray is parameterized by $y = (\beta, \gamma) \in \tilde{Y}$. The ideal, continuous-domain, point-spread functions for these three geometries are

$$\begin{aligned} h(y|x) &\equiv h(t, \varphi|x_1, x_2) \\ &= \delta(t - x_1 \cos\varphi - x_2 \sin\varphi) \end{aligned} \tag{19}$$

$$\begin{aligned} h(y|x) &\equiv h(\beta, \gamma|x_1, x_2) \\ &= \delta[D \sin\gamma - x_1 \cos(\beta + \gamma) \\ &\quad - x_2 \sin(\beta + \gamma)] \end{aligned} \tag{20}$$

and

$$\begin{aligned} h(y|x) &\equiv h(\beta, \gamma|x_1, x_2, x_3) \\ &= \delta[D \sin\gamma - x_1 \cos(\beta + \gamma) - x_2 \sin(\beta + \gamma)] \\ &\quad \times \delta(x_3 - p\beta) \end{aligned} \tag{21}$$

respectively, where p is the helical pitch. These idealized point-spread functions can be modified readily to account for the finite sizes of an X-ray source and detector. The discrete model (1) is derived from this continuous model by discretizing the spaces, $\tilde{X}$ and $\tilde{Y}$, and then approximating line integrals along projection rays in the discrete spaces by linear, bilinear, or other choices of interpolation. Suitable choices for the parameter space Θ are described above in Section II.

The summation

$$\sum_{x'} h(y|x') \hat{c}^{(k)}(x') \tag{22}$$

appearing in (17) is the forward projection of the stage k reconstruction, $\hat{c}^{(k)}(\cdot)$, of the attenuation coefficient distribution, $c(\cdot)$, where the forward projection is through the model point-spread function of the tomograph. From (17), the ratio of the projection data, $m(\cdot)$, and this forward projection is then linearly transformed via a kernel that is the adjoint of the model point-spread function according to

$$\sum_{y \in Y} h(y|x) \left[\frac{m(y)}{\sum_{x'} h(y|x') \hat{c}^{(k)}(x')} \right]. \tag{23}$$

This can be interpreted as the image formed by back projecting the ratio function. Thus, both forward and backward projections are required in forming reconstructions using our method, and these must be repeated at each stage of the iterations.

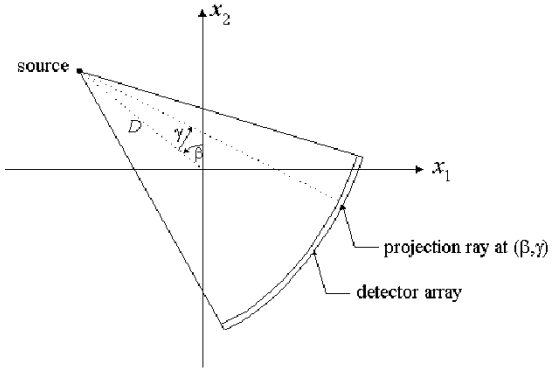

Fig. 1. CT fan-beam geometry.

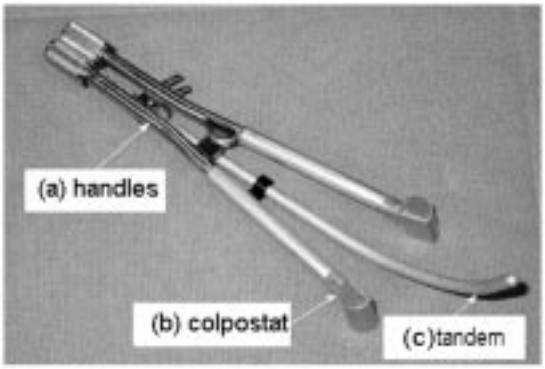

Fig. 2. Fletcher–Suit–Delclos intracavitary applicators. Three ceramic cylinders of length 20 mm containing Cs-137 are loaded end-to-end in the tandem, and one such source is loaded along each ovoid axis. (a) Handles. (b) Colpostat. (c) Intrauterine tandem. The length of the applicator is approximately 20 cm from handle to ovoid tips.

V. Application to Brachytherapy

Brachytherapy is used for a variety of surgically accessible local malignancies. It consists of placing one or more sealed radioactive sources very close to or in contact with the target tissue, allowing large doses of radiation to be safely delivered to the target volume [29]. A variety of devices or applicators are used to contain the radioactive source, including seeds, needles, and intracavitary colpostats. Shown in Fig. 2 is an example of an intracavitary system used to treat locally advanced cervical cancer. This particular applicator is specially constructed for our research program. As described by Weeks and Montana [28], the colpostat's body consists of aluminum. This applicator contains retractable tungsten-alloy shields, whose purpose is to reduce the dose delivered to bladder and rectal tissue. During an intracavitary procedure, the applicators in Fig. 2 without radioactive sources or tungsten shields are surgically positioned in the patient. The intrauterine tandem is inserted through the cervical os into the uterine canal. The colpostats are placed in the lateral vaginal fornices just below the cervical os. After imaging the applicator system, the radioactive sources along with tungsten shields are afterloaded into the applicator via channels in the colpostat and tandem handles. The loaded applicator system is left in place, usually for 24–72 h, until the prescribed dose

is delivered. Since the experimental applicators shown in Fig. 2 consist only of aluminum components in their unloaded configuration, relatively artifact-free CT images showing the implant location relative to the pelvic soft-tissue structures can be obtained. However, commercially available intrauterine tandems and vaginal colpostats are fabricated from stainless steel and have tungsten shielding and other heavy metal components permanently fixed in the colpostats. CT imaging performed with such applicators in place yields very poor quality images with significant artifacts masking soft-tissue regions.

Locally advanced cervical cancer is treated with a combination of external radiation delivered by high-energy X-ray beams and by brachytherapy [15]. The five-year survival rate for women with stage III disease is approximately 50%, which motivates seeking ways for improvement. The brachytherapy portion of the treatment is performed by highly skilled radiation oncologists but remains an art. One limitation to improving this form of treatment is that artifact-free, volumetric images showing patient anatomy in relation to the implanted applicator are not presently available to the oncologist via computed tomography based on conventional FBP for most types of applicators because of strong artifacts. The location of the applicator relative to the malignancy and nearby sensitive structures is usually surmised from orthogonal X-ray projections. As a result, accurate estimates of the radiation dose delivered to the target volume and sensitive structures, such as the bladder and rectum, are difficult to make with a high degree of confidence. With this as motivation, we have initiated a project to make such images available, with the goal being to achieve accurate dose predictions and an improved survival rate.

Applicators are man-made, so engineering drawings and specifications for them are available (see [28] for example), and this information is what we seek to exploit while reconstructing tomographic images. Let $\{c_a(x), x \in X\}$ be a function describing the applicator's attenuation coefficient in a reference pose. This function encapsulates the known geometric and X-ray attenuation characteristics of the applicator at the scanner's energy. We assume that a representation of this function is stored in computer memory for use in the image formation method we have described. The applicator function is moved via rotation and translation to its estimated position in the cervix, where it is described with a rotation matrix and translation vector, $\theta = (R, x_0)$, as $\{c_a(Rx + x_0), x \in X\}$.

The attenuation function, $\{c(x), x \in X\}$, of the pelvic region with the applicator in place is modeled as in (3), with $\{c_b(x), x \in X\}$ representing the attenuation map of the pelvic tissues and structures that surround the applicator.

We have performed preliminary experiments to test the efficacy of OCCT for improving tomographic images to be used in the brachytherapy treatment of advanced cervical cancer. CT images in the several figures that follow have the same viewing window (i.e., gray-scale thresholds), with white areas showing attenuation coefficient of 0.035 mm^{-1} or higher, corresponding to $+400$ Hounsfield units, and black areas showing regions with attenuation of 0.015 mm^{-1} or less, corresponding to -400 Hounsfield units. The dimension of these images in pixels is 512×512, with each pixel being a square of 1 mm/side. Projection sinograms are in a planar, fan-beam geometry with

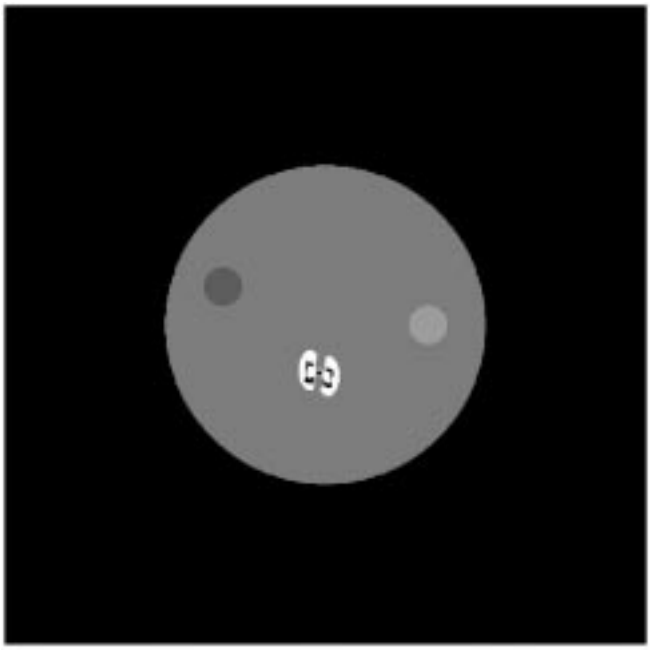

Fig. 3. Synthetic phantom showing applicator in water and two circular regions having attenuation values of -10% and $+10\%$ that of water.

768 detectors and 1408 source angles/rotation. These values of pixelization and data-acquisition sampling are consistent with those of commercial CT scanners, so aliasing artifacts that result are comparable to those present in images reconstructed on commercial scanners.

Shown in Fig. 3 is the phantom used to produce synthetic projection data for the experiments. It consists of a circular region of water (0.025 mm^{-1}) in which a planar section through the colpostats and tandem shown in Fig. 2 and two circular regions with attenuation $+10\%$ and -10% that of water are embedded. The applicator section includes aluminum, tungsten, ceramic, and air parts. Synthetic fan-beam sinogram data were then produced by performing forward projections numerically on these phantoms, assuming monoenergetic X-ray radiation. The methods we use for producing these forward projections and for the backprojections required in the reconstructions are described by Politte and Whiting [16]. These synthetic data were then processed in a variety of ways.

Experiment 1: (FBP): Synthetic sinogram data derived from the phantom of Fig. 3 were processed using FBP, which ignores the presence of the applicator or knowledge of any of its properties, yielding the result in Fig. 4. Streaking artifacts due to the high-density applicator are evident. These artifacts are substantially less severe than those produced by actual CT scanners in the presence of high-density metal. We conjecture that this is due to beam hardening, photon-scatter, and noise effects that are ignored in our linear model and the assumption made here of noise-free monoenergetic projections. Aliasing due to finite pixelization and data-acquisition sampling also contribute to the artifacts seen. As mentioned before, artifacts due to aliasing are comparable to those encountered with commerical CT scanners.

Experiment 2: (OCCT With Known Applicator Pose): The synthetic sinogram data derived from the phantoms of Fig. 3 were processed by iterating (16) for 300 steps but with the appli-

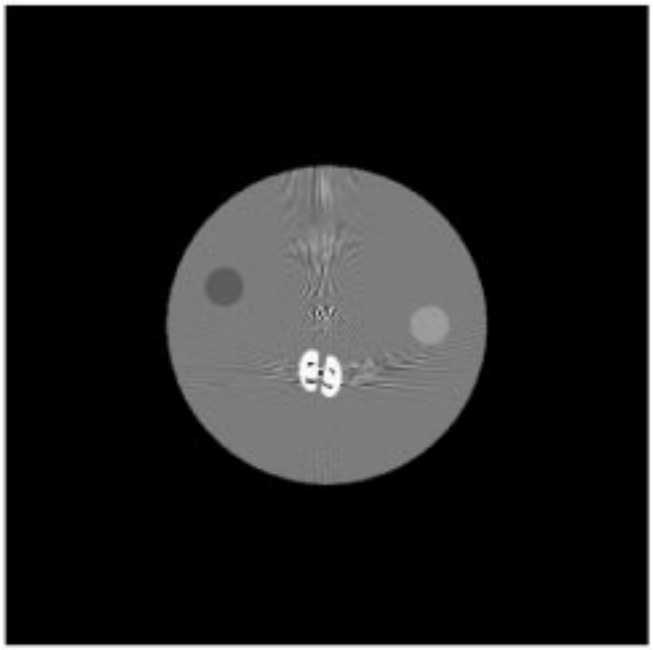

Fig. 4. Reconstructed image for the phantom of Fig. 3 using FBP.

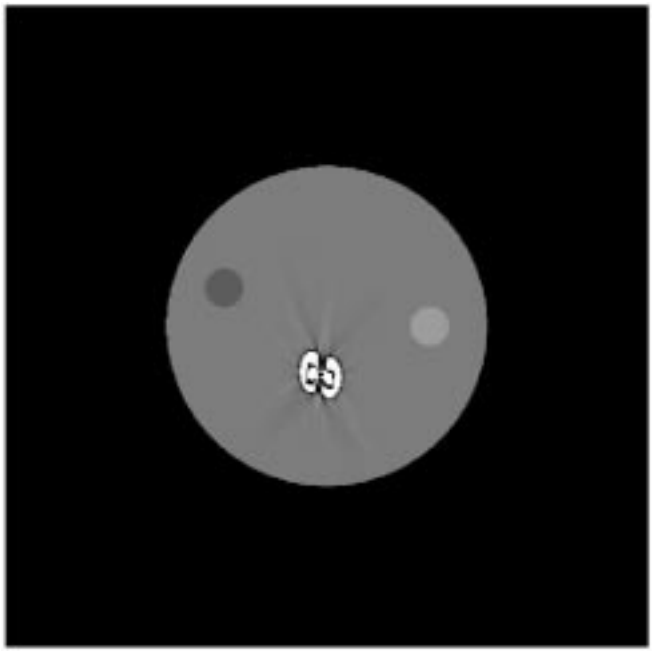

Fig. 5. Reconstructed image using OCCT with applicator fixed at true pose for the phantom of Fig. 3.

cator held fixed precisely at its correct position and orientation (that is, with $\theta = \theta_{\text{true}}$). The result is in Fig. 5. The streaking artifacts evident in Fig. 4 are seen to be suppressed, showing that accounting for the applicator can lead to significant improvement in the quality of the reconstructed image. This result is similar to but extends that reported in [17], [22], and [26], wherein a uniformly opaque, convex applicator model was used and assumed to be in a known pose, to include a nonuniform applicator with parts having finite attenuation coefficients.

Experiment 3: (OCCT With Unknown Applicator Pose): In this experiment, the synthetic sinogram data for both phantoms were processed by iterating (12)–(14) for 300 steps. The initial condition of the pose (11) was determined via ten steps of a gradient search to solve the minimization in (13) with the estimate of the body attenuation coefficient, $\hat{c}_b^{(0)}(x)$, held uniformly constant.[2] The result, shown in Fig. 6, is quite close but not identical to that of Experiment 2 in Fig. 5. This is explained by the estimated pose parameters resulting from the iterations leading to Fig. 6 being close to the true pose parameters used in reaching Fig. 5: the estimated parameters are $\hat{\theta} = (-5.183$ mm, -38.6403 mm, 100.7056 degrees), and the true parameters are $\theta_{\text{true}} = (-5.178$ mm, -38.635 mm, 100.72 degrees) Another comparison of the results of these experiments is shown in Fig. 7, where a profile through the reconstruction is given at a location slightly outside the applicator where a malignancy might be encountered, as shown in Fig. 8. The true attenuation coefficients used in the simulation are shown along with their estimated values obtained in this experiment.

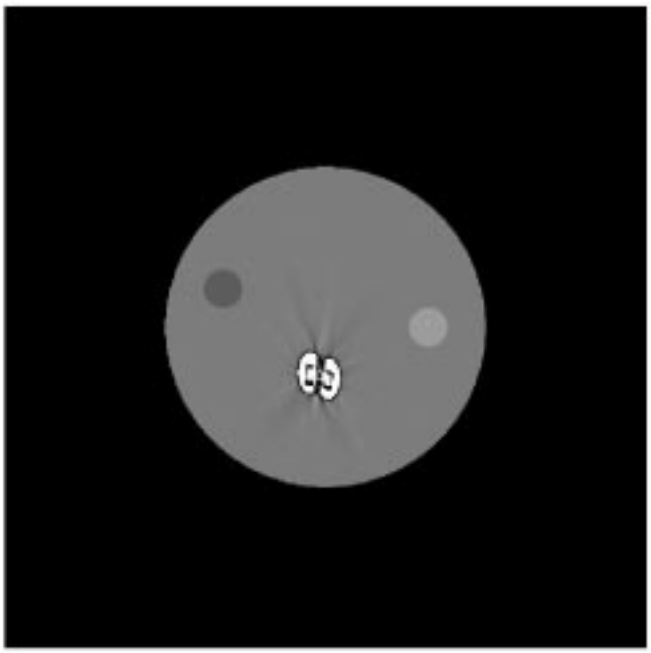

Fig. 6. Reconstructed image using OCCT with applicator pose estimated concurrently with the image reconstruction for the phantom of Fig. 3.

The results of these experiments are encouraging to us, but it is difficult at this time to predict what will be obtained when the full 3-D implementation of our approach is completed and tested. This full implementation is presently being developed and will accommodate objects that have a nonuniform attenuation characteristic and are not in a known pose. Also, volumetric, spiral CT data will be included.

VI. Conclusion

We have described a new approach for solving linear deblurring problems when the function sought has a component that is known to within a set of parameters. When applied to tomographic imaging, this approach leads to a method for accom-

[2]An alternative method for determining an initial estimate of the pose is to use the method described by Weeks [27] wherein a scan-set of CT images is segmented to estimate the pose of an applicator. We have not attempted this alternative in favor of an approach in which the applicator pose and body reconstruction are performed automatically in the coordinated framework we have described.

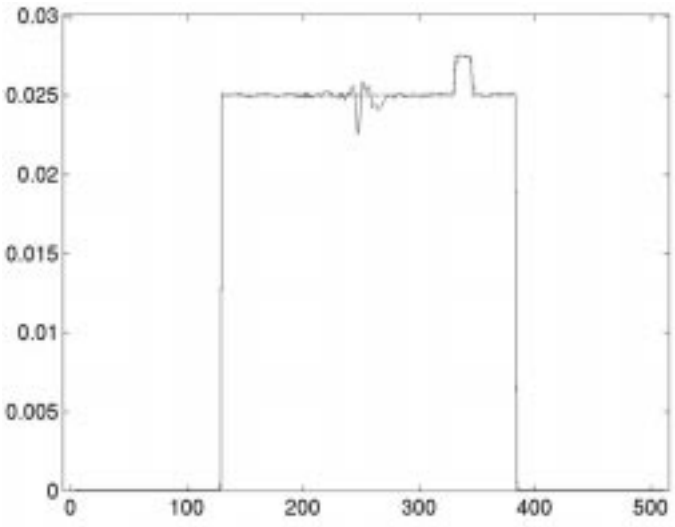

Fig. 7. Profiles through the true image (dashed) of Fig. 3 and the reconstructions (solid) of Fig. 6.

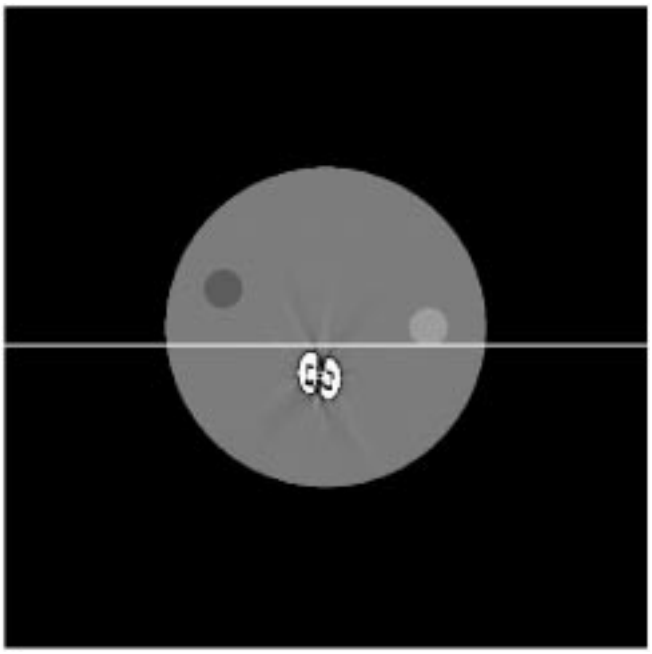

Fig. 8. Image of Fig. 6 with the location of the profiles of Fig. 7 indicated.

modating all that is known about man-made foreign objects that may be inside the body, resulting in improved images with fewer artifacts than those obtained with FBP.

This image formation method we have described extends the work of Wang *et al.* [26] in two directions. The first is the inclusion of parameters in the object model, which for tomographic imaging permits an unknown location and orientation of the object to be considered. Second, the object can have an arbitrary attenuation characteristic, so it does not need to be totally opaque as in [26]. In the case of a totally opaque object with a known location and orientation, the method we have described for Experiment 2 and that in [26] are identical.

We have described a preliminary experiment that suggests that the artifacts seen in tomographic images when high-density metal objects are present can be greatly decreased. We anticipate that ongoing experiments will confirm that this improvement is maintained in more realistic situations where applicators are 3-D and data are acquired in volumetric spiral-CT scans. If so, we expect that our method will be of benefit to other applications besides brachytherapy where man-made foreign objects are present in the body, including orthopedic implants, surgical clips, spinal braces, dental restorations, and cochlear implants.

Although the modeling of X-ray tomographic imaging as a deterministic, linear deblurring problem is a common choice, it has limitations. Real projection data acquired with an X-ray tomograph exhibit both photon-fluctuation noise and beam hardening effects and can be modeled more accurately, but still with limitations, as a Poisson process with a mean-value function of the form

$$\sum_E I_0(y,E)\exp\left(-\sum_{x\in X} h(y|x)c(x:E)\right) \qquad (24)$$

where $I_0(y,E)$ is the energy-dependent intensity of the X-ray source, and $c(x:E)$ is the energy-dependent attenuation function. For a monoenergetic, unit-intensity source, the negative logarithm of this mean-value function yields the linear model in (1). In developing the OCCT approach, we have as a first approximation assumed a monoenergetic source and ignored noise to facilitate addressing how to accommodate known characteristics of objects in the field of view. We have, therefore, assumed that real projection data equal their mean-value function, taken the negative logarithm, and minimized I-divergence for the linear model (1). The effects of noise and beam hardening on the linear-based OCCT approach are presently under study and will be reported when complete. The I-divergence (7) is, to within a constant, the negative loglikelihood functional for Poisson-distributed data with a mean-value function equal to $\sum_{x\in X} h(y|x)c(x)$, and (17) is the expectation-maximization (EM) algorithm for such data encountered in emission tomography, as given by Shepp and Vardi [20]; that this result is obtained is a consequence of using the linear model (1). We are also developing an extended OCCT approach that accounts fundamentally for photon-fluctuation noise, beam hardening present with a polyenergetic source, and photon scatter [14]. This is based on maximizing the Poisson loglikelihood for transmission tomography as given by Lange and Carson [9] but extended to include beam hardening and scatter effects.

APPENDIX
DERIVATION OF (12)–(14)

From the definition in (8)

$$\sum_{x\in X} P(x|y:\tilde{c}(\cdot)) = 1, \qquad \text{for all } y\in Y. \qquad (25)$$

It follows from this that:

$$\ln\left[\sum_{x\in X} h(y|x)c(x)\right] = \sum_{x\in X} P(x|y:\tilde{c}(\cdot)) \times \{\ln c(x) + \ln h(y|x) - \ln P(x|y:c(\cdot)\}. \qquad (26)$$

Substitution of this expression into (7) and rearranging terms yields

$$\begin{aligned} I(c(\cdot)) = &- \sum_{y\in Y}\sum_{x\in X} m(y)P\left(x|y:\tilde{c}(\cdot)\right)\ln c(x) \\ &+ \sum_{y\in Y}\left[\sum_{x\in X} h(y|x)c(x) - m(y)\right] \\ &+ \sum_{y\in Y} m(y)\left[\ln m(y) - \sum_{x\in X} P\left(x|y:\tilde{c}(\cdot)\right)\ln h(y|x)\right] \\ &+ \sum_{y\in Y} m(y)\sum_{x\in X} P\left(x|y:\tilde{c}(\cdot)\right)\ln P\left(x|y:c(\cdot)\right) \end{aligned} \tag{27}$$

where $\tilde{c}(\cdot)$ and $c(\cdot)$ are admissible images for poses $\tilde{\theta}$ and θ, respectively.

We need to demonstrate that the iteration defined in (12)–(14) produces a nonincreasing sequence of I-divergences $I(c)$. Consider the difference

$$I\left(\hat{c}^{(k)}\right) - I\left(\hat{c}^{(k+1)}\right). \tag{28}$$

Set $\tilde{c}(x) = \hat{c}^{(k)}(x)$, $x \in X$, in (27), and use $\hat{c}^{(k)}(x) = \hat{c}^{(k)}(x : \hat{\theta}^{(k)})$ from (14). The contribution of the first two terms on the right—hand side of (27) to the difference in (28) is

$$\begin{aligned} &- \sum_{y\in Y}\sum_{x\in X} m(y)P\left(x|y:\hat{c}^{(k)}(\cdot)\right)\ln \hat{c}^{(k)}\left(x:\hat{\theta}^{(k)}\right) \\ &+ \sum_{x\in X} H_0(x)\hat{c}^{(k)}\left(x:\hat{\theta}^{(k)}\right)\Big) \\ &+ \sum_{y\in Y}\sum_{x\in X} m(y)P\left(x|y:\hat{c}^{(k)}(\cdot)\right)\ln \hat{c}^{(k+1)}\left(x:\hat{\theta}^{(k+1)}\right) \\ &- \sum_{x\in X} H_0(x)\hat{c}^{(k+1)}\left(x:\hat{\theta}^{(k+1)}\right) \\ \geq &- \sum_{y\in Y}\sum_{x\in X} m(y)P\left(x|y:\hat{c}^{(k)}(\cdot)\right)\ln \hat{c}^{(k)}\left(x:\hat{\theta}^{(k)}\right) \\ &+ \sum_{x\in X} H_0(x)\hat{c}^{(k)}\left(x:\hat{\theta}^{(k)}\right)\Big) \\ &+ \sum_{y\in Y}\sum_{x\in X} m(y)P\left(x|y:\hat{c}^{(k)}(\cdot)\right)\ln \hat{c}^{(k+1)}\left(x:\hat{\theta}^{(k)}\right) \\ &- \sum_{x\in X} H_0(x)\hat{c}^{(k+1)}\left(x:\hat{\theta}^{(k)}\right) \\ \geq &\ 0 \end{aligned} \tag{29}$$

where the first inequality follows from the definition of $\hat{\theta}^{(k+1)}$ in (13) as a minimizer, and the second inequality follows from the definition of $\hat{c}^{(k+1)}(x:\hat{\theta}^{(k)})$ in (12) as a minimizer for any choice of θ including $\hat{\theta}^{(k)}$. The third term on the right in (27) cancels in the difference in (28). The contribution of the last term on the right in (27) to the difference in (28) is

$$\sum_{y\in Y} m(y)\sum_{x\in X} P\left(x|y:\hat{c}^{(k)}(\cdot)\right)\ln\left[\frac{P\left(x|y:\hat{c}^{(k)}(\cdot)\right)}{P\left(x|y:\hat{c}^{(k+1)}(\cdot)\right)}\right]. \tag{30}$$

That this difference is nonnegative follows from (25) and the inequality $\ln(1/\xi) \geq 1-\xi$. Thus, the difference in (28) is nonnegative, so the sequence of image estimates produced by (12)–(14) yields a nonincreasing sequence of I-divergences.

ACKNOWLEDGMENT

The authors are grateful to P. Amin, J. Blaine, J. Dempsey, M. Jonsson, and F. Lerma for their help with the experiments we described. They appreciate the comments and suggestions made by anonymous reviewers of our manuscript because these led to significant improvements in the OCCT approach.

REFERENCES

[1] C. L. Byrne, "Iterative image reconstruction algorithms based on cross-entropy minimization," *IEEE Trans. Image Processing*, vol. 2, pp. 96–103, Jun. 1993.

[2] I. Csiszár, "Why least squares and maximum entropy? An axiomatic approach to inference for linear inverse problems," *Ann. Stat.*, vol. 19, pp. 2032–2066, 1991.

[3] B. D. DeMan, J. Nuyts, P. Dupont, G. Marchal, and P. Suetens, "Metal streak artifacts in X-ray computed tomography: A simulation study," presented at the IEEE Nuclear Science Symp. and Medical Imaging Conf., Toronto, Canada, 1998.

[4] T. G. S. Fiala, R. A. Novelline, and M. J. Yaremchuk, "Comparison of CT imaging artifacts from craniomaxillo facial internal fixation devices," *Plastic Reconstr. Surg.*, vol. 92, pp. 1227–1232, 1993.

[5] W. J. Gebara, K. J. Weeks, and C. A. Hahn, "Computed axial tomography tandem and ovoids (CATTO) dosimetry: Three-dimensional assessment of bladder and rectal doses," *Radiat. Oncol. Investigat.*, vol. 6, pp. 268–275, 1998.

[6] G. H. Glover and N. J. Pelc, "An algorithm for the reduction of metal clip artifacts in CT reconstructions," *Med. Phys.*, vol. 8, pp. 799–807, 1981.

[7] W. A. Kalender, R. Hebel, and J. Ebersberger, "Reduction of CT artifacts caused by metallic implants," *Radiology*, vol. 164, pp. 576–577, 1987.

[8] E. Klotz and W. Kalender, "Algorithms for the reduction of CT artifacts caused by metallic implants," *Proc. SPIE*, vol. 1234, pp. 642–650, 1990.

[9] K. Lange and R. Carson, "EM reconstruction algorithms for emission and transmission tomography," *J. Comput. Assist. Tomogr.*, vol. 8, pp. 306–316, 1984.

[10] A. H. R. Lonn and C. R. Crawford, "Reduction of artifacts caused by metallic objects in CT," *Radiology*, vol. 169(P), p. 116, 1988.

[11] W. M. Marks and P. W. Callen, "Computed tomography in the evaluation of patients with surgical clips," *Surg. Gynecol. Obstet.*, vol. 151, pp. 557–558, 1980.

[12] J. A. O'Sullivan, "Alternating minimization algorithms: From Blahut–Arimoto to expectation-maximization," in *Codes, Curves, and Signals—Common Threads in Communications*, A. Vardy, Ed. Norwell, MA: Kluwer Academic, 1998, pp. 173–192.

[13] J. A. O'Sullivan, R. E. Blahut, and D. L. Snyder, "Information-theoretic image formation," *IEEE Trans. Inform. Theory*, vol. 44, pp. 2094–2123, Oct. 1998.

[14] J. A. O'Sullivan and J. Benac, "Alternating minimization algorithms for transmission tomography," IEEE Trans. Med. Imag., June 2001, submitted for publication.

[15] C. A. Perez, "Uterine cervix," in *Principles and Practice of Radiation Oncology*, 3rd ed, C. A. Perez and L. W. Brady, Eds. Philadelphia, PA: Lippencott-Raven, 1998, ch. 62, pp. 1733–1834.

[16] D. G. Politte and B. R. Whiting, "A fast, accurate projector/backprojector pair for use with iterative image reconstruction for two-dimensional fan-beam transmission imaging," *IEEE Trans. Med. Imag.*, July 2001, submitted for publication.

[17] D. D. Robertson, J. Yuan, G. Wang, and M. W. Vannier, "Total hip prosthesis metal-artifact suppression using iterative deblurring reconstruction," *J. Comput. Assist. Tomogr.*, vol. 21, pp. 293–298, 1997.

[18] D. D. Robertson, P. J. Weiss, E. K. Fishman, D. Magid, and P. S. Walker, "Evaluation of CT techniques for reducing artifacts in the presence of metallic orthopedic implants," *J. Comput. Assist. Tomogr.*, vol. 12, pp. 236–241, 1988.

[19] T. Rohlfing, D. Zerfowski, J. Beier, P. Wust, N. Hosten, and R. Felix, "Reduction of metal artifacts in computed tomographies for the planning and simulation of radiation therapy," presented at the Computer Assisted Radiology Conf., Tokyo, Japan, June 1998.

[20] L. A. Shepp and Y. Vardi, "Maximum likelihood reconstruction for emission tomography," *IEEE Trans. Med. Imag.*, vol. MI-1, pp. 113–122, 1982.

[21] D. L. Snyder, T. J. Schulz, and J. A. O'Sullivan, "Deblurring subject to nonnegativity constraints," *IEEE Trans. Signal Processing*, vol. 40, pp. 1143–1150, May 1992.

[22] D. L. Snyder, M. Joshi, J. A. O'Sullivan, J. F. Williamson, C. K. S. Chao, and G. Wang, "Spiral x-ray CT imaging in the presence of high-density brachytherapy applicators," presented at the IEEE Medical Imaging Conf. (poster), Albuquerque, NM, Nov. 1997.

[23] H. Stark, Ed., *Image Recovery, Theory, and Applications*. New York: Academic, 1987.

[24] N. Strumas, O. Antonyshyn, M. J. Yaffe, G. Mawdsley, and P. Cooper. Computed tomography artifacts: An experimental investigation of causative factors. presented at 49th Annu. Meeting the Canadian Society of Plastic Surgeons. [Online]. Available: http://www.pulsus.com/plastics/06_01/stru_ed.htm

[25] Y. Vardi and D. Lee, "From image deblurring to optimal investments: Maximum-likelihood solutions to positive linear inverse problems," *J. Roy. Statist. Soc., B*, pp. 569–612, 1993.

[26] G. Wang, D. L. Snyder, J. A. O'Sullivan, and M. W. Vannier, "Iterative deblurring for CT metal artifact reduction," *IEEE Trans. Med. Imag.*, vol. 15, pp. 657–664, Oct. 1996.

[27] K. J. Weeks, "Brachytherapy object-oriented treatment planning based on three dimensional image guidance," in *Categorical Course in Brachytherapy Physics*, B. Thomadsen, Ed. Oakbrook, IL: RSNA, 1997, pp. 79–86.

[28] K. J. Weeks and G. S. Montana, "Three-dimensional applicator system for carcinoma of the uterine cervix," *Int. J. Radiation Oncol. Biol. Phys.*, vol. 37, pp. 455–463, 1997.

[29] J. F. Williamson, "Physics of brachytherapy," in *Principles and Practice of Radiation Oncology*, 3rd ed, C. A. Perez and L. W. Brady, Eds. Philadelphia, PA: Lippencott-Raven, 1998, ch. 15, pp. 405–468.

[30] D. C. Youla, "Mathematical theory of image restoration by the method of convex projections," in *Image Recovery, Theory, and Applications*, H. Stark, Ed. New York: Academic, 1987, ch. 2.